Reverberant Room-to-Room Radio Channel Prediction by Using Rays and Graphs

Miao, Yang; Pedersen, Troels; Gan, Mingming; Vinogradov, Evengenii; Oestges, Claude

Published in:
I E E E Transactions on Antennas and Propagation

DOI (link to publication from Publisher):
10.1109/TAP.2018.2878088

Publication date:
2019

Document Version
Accepted author manuscript, peer reviewed version

Reverberant Room-to-Room Radio Channel Prediction by Using Rays and Graphs

Yang Miao, Troels Pedersen, Mingming Gan, Evgenii Vinogradov, and Claude Oestges

***Abstract*—This paper proposes a hybrid modeling approach for prediction of the room-to-room radio propagation channel. The model combines ray tracing with propagation graph. The propagation graph vertices are obtained at each room by ray tracing with the assumption that the receive antenna (or transmit antenna) virtually locates on the surface of the separating wall between two rooms. Rays transmitted from one room to the other through the separating wall are deterministically calculated by Snell's law of refraction. Predictions by the proposed model are compared with measurement data from an office-to-office scenario. The results show that the proposed modeling works with the simplest parameter settings, i.e. assuming no propagation from the room containing receive antenna to the room containing transmit antenna, ray tracing applied separately in each room only involves mechanism of line-of-sight and first order specular reflection.**

***Keywords*—Room-to-Room Radio Channel, Ray Tracing, Propagation Graph**

I. Introduction

The dense multipath components (DMC) of indoor scenarios are composed of area diffuse components and a reverberant part consisting of a multitude of specular components [1], [2], [3], [4], [5]. While the diffuse scattering is mostly caused by macroscopically rough surfaces, the reverberant part of DMC, described as the diffuse tail [6] [7], [8], stems from multiple scattering which occurs for closed environments no matter if the walls are rough or not. Typically, single bounce diffuse scattering alone is insufficient to account for the observed diffuse tail. In practice, multiple specular scattering or multiple diffuse scattering better describes the phenomenon but is unfeasible in many cases due to a high computational complexity [9], [10], [11]. Remarkably most of the computational effort is spent on calculating with high accuracy the myriad of low powered contributions constituting the diffuse tail [12], [13], [14]. This seems wasteful since for most applications the very high accuracy of each of these individual components is not required.

One of the sound approaches for modeling the diffuse tail is the so-called propagation graph (PG) models [9], [15]. In a PG, the vertices represent transmitters, receivers and scatterers presenting in the propagation environment. The edges model propagation between vertices. The transfer function of a PG is available in closed form and can be computed even if infinitely many occur. This feature eliminates the need for upper bounding the number of interactions considered in a PG. While the surface roughness in propagation environment may impact the choice of the scattering points in PG models, the major effect captured in PG is the time-dispersion due to the propagation delays among surface interactions. Stochastic generation of PG has successfully predicted the in-room [9] and outdoor-to-indoor [15] radio channels. In [16], a PG model was proposed to include the human body shadowing effect in indoor channel modeling. The contribution [17] utilizes PG to model the multi-bounce diffuse components and uses a single-lobe directive model to reproduce individual single-bounce specular components together with diffuse components associated for in-room scenario.

Hybrid approaches where PG and ray tracing (RT) are combined have also been proposed for the in-room radio channel [10], [18]. In [18], the reverberation tail is modeled as multi-bounce specular scattering. To simplify the RT, a PG is constructed by considering scattering points on the reflection points derived from RT. The parameter settings are meant to illustrate the diffusion effect in in-room scenarios, although it requires to adjust and train the parameters according to the evaluation with measurement data. In [10], the reverberation is described by multi-bounce of diffuse scattering. The authors place scatterers according to a given distribution on wall surfaces and/or building volume, and adopt multi-bounce effective roughness (ER) Lambertian model [12] to PG to make the model physically sound. The computational complexity is increased especially for large indoor scenarios. In addition, the more realistic ER directive model is difficult to adopt here since it requires us to keep track of the exact trajectory of paths within the graph model.

For more complex room-to-room environments where transmit antenna (Tx) and receive antenna (Rx) reside in adjacent rooms, a more detailed structure of PGs should be devised. In the studies of room electromagnetics, the diffuse tail for Rx being in the same room as Tx and that for Rx being in the adjacent room are analyzed based on measurement data [19], [20]. However, to the best of our knowledge, the room-to-room radio channel prediction has not yet been deterministically and efficiently fulfilled by taking advantage of the recursive structure of PG; solving this issue will certainly bring benefit to the indoor wireless network planning. To model the channel, using RT alone for room-to-room scenario is computation-intensive because of the reverberant DMC in both rooms;

Y. Miao and C. Oestges are with the Institute of Information and Communication Technologies, Electronics and Applied Mathematics (ICTEAM), Universite Catholique de Louvain, Place du Levant 3, B-1348, Louvain-la-Neuve, Belgium, e-mail: {yang.miao, claude.oestges}@uclouvain.be. E. Vinogradov is with the TELEMIC, Department of Electrical Engineering, Katholieke Universiteit Leuven, Kasteelpark Arenberg 10, B-3100, Leuven, Belgium, e-mail: evgenii.vinogradov@kuleuven.be. T. Pedersen is with the Department of Electronic Systems, Section Wireless Communication Networks, Aalborg University, Aalborg, 9220, Denmark, e-mail: troels@es.aau.dk. M. Gan is with the Department of Research and Development on Wireless Radio Product, Huawei, Shanghai, China, e-mail: mingminggan@huawei.com.

however, using PG requires the information of interaction points between radio waves and physical scatterers which could be obtained from RT. Hence our interest is to solve the issues of computation inefficiency and interaction points for room-to-room scenario by using RT and PG in combination. Our devised hybrid approach differs from the hybrid approach in [10], [18] where the output from RT and PG are added; the motivation of our approach is to efficiently use the output information of the scatterers' interactive points from RT for the calculation of PG.

This paper proposes an accurate modeling approach using PG and RT to predict the room-to-room radio channel. The contributions are twofold.

First, a hybrid model utilizing both RT and PG is proposed. PG vertices are the interactive points obtained by applying RT separately to each room. In the room containing Tx, RT is applied by assuming that Rx is virtually located on the surface of the separating wall. The pseudo-Rx locations are deployed uniformly on the wall surface. The undisturbed line, or the pseudo line-of-sight (LOS) in other words, and the specular reflection (SR) paths between Tx and pseudo-Rx are calculated by RT considering all objects in the room containing Tx except for the separating wall surface. Paths through the separating wall are calculated deterministically by Snell's refraction law. In the room containing Rx, RT is applied by assuming that Tx is virtually located on the surface of the separating wall, and the pseudo-Tx locations are the locations that the transmitting-through paths arrive on. PG edges are constructed by connecting the interactive points of pseudo-LOS and SR paths in the room containing Tx, the pseudo-Rx and pseudo-Tx positions, and the interactive points of pseudo-LOS and SR paths in the room containing Rx. Channel transfer function is obtained by endowing edge transfer function for all edges.

Second, the proposed modeling approach is applied in a real-world scenario of typical office rooms, and is evaluated by comparing with the measured data as well as the data predicted by using only the conventional RT tools. In this measurement, the power delay profile (PDP) as one of the most important parameter in room-to-room radio channel prediction is addressed. The investigating parameters include the PDP discrepancy, the mean delay, the root mean square (r.m.s.) delay spread, and the time consumption. Through analysis of the resulting PDP from different modeling parameter settings in the proposed approach, the validity and the applicability of the proposed modeling are verified.

The rest of the paper is as follows. In Section II, the proposed modeling algorithm is presented. In Section III, the measurement campaign is described. In Section IV, the validation is discussed and numerical examples are presented. Section V concludes this paper.

II. Hybrid Model for Predicting Room-to-Room Radio Channel

A. Propagation Graph for Room-to-Room Scenario

We now set up a PG for the scenario shown in Fig. 1 where N_{t} Tx antennas sitting in Room $\mathcal{R}_{\mathrm{t}} \subset \mathbb{R}^3$ communicates to

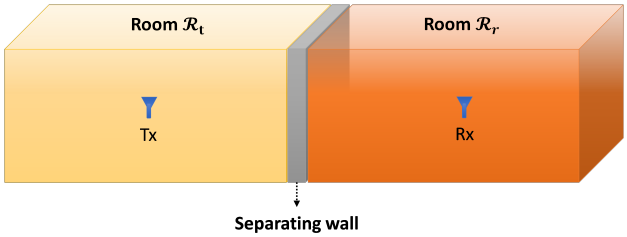

Fig. 1. Schematic diagram for the considered room-to-room scenario when Tx and Rx are in adjacent rooms

the N_{r} Rx antennas located in the adjacent room $\mathcal{R}_{\mathrm{r}} \subset \mathbb{R}^3$ separated by a wall. A position vector $\boldsymbol{r}_v \in \mathbb{R}^3$ is associated to each vertex $v \in \mathcal{V}$. The set of scatterers can be split as $\mathcal{V}_{\mathrm{S}} = \mathcal{V}_{\mathrm{S_t}} \cup \mathcal{V}_{\mathrm{S_r}}$ where scatterers $\mathcal{V}_{\mathrm{S_t}}$ positions are in $\mathcal{R}_{\mathrm{t}}$ and scatterers $\mathcal{V}_{\mathrm{S_r}}$ positions are in $\mathcal{R}_{\mathrm{r}}$. N_{t} is the total number of Tx, N_{r} is the total number of Rx, $N_{\mathrm{S_t}}$ is the total number of $\mathcal{V}_{\mathrm{S_t}}$, and $N_{\mathrm{S_r}}$ is the total number of $\mathcal{V}_{\mathrm{S_r}}$.

Following [9], [15], [18], the edges of the graph are defined as follows. First, since Tx and Rx are separated by a wall, no direct propagation occurs, i.e. $D(f) = 0$. Furthermore, we assume that Tx have edges to scatterers $\mathcal{V}_{\mathrm{S_t}}$, and scatterers $\mathcal{V}_{\mathrm{S_t}}$ have edges to other scatterers $\mathcal{V}_{\mathrm{S_t}}$. We also assume that scatterers $\mathcal{V}_{\mathrm{S_t}}$ and scatterers $\mathcal{V}_{\mathrm{S_r}}$ can be connected by edges through the separating wall, which is based on the assumption that the separating wall is penetrable. Moreover, we assume scatterers $\mathcal{V}_{\mathrm{S_r}}$ have edges to other scatterers $\mathcal{V}_{\mathrm{S_r}}$ and also to the Rx. Note that we neglect the signals which leave the rooms and there is no edge between scatterers on the same wall. These considerations lead to the vector signal flow graph representing the PG shown in Fig. 2.

The input signal vector is $\boldsymbol{X}(f) = [X_1(f), \ldots, X_{N_{\mathrm{t}}}(f)]^{\mathrm{T}}$, with $X_m(f)$ denoting the frequency domain signal emitted by transmitter Tx_m, and $[\cdot]^T$ denotes the transposition operator. The output signal vector is $\boldsymbol{Y}(f) = [Y_1(f), \ldots, Y_{N_{\mathrm{r}}}(f)]^{\mathrm{T}}$, with $Y_m(f)$ denoting the signal observed by receiver Rx_m. Similarly, $\boldsymbol{Z}_{\mathrm{t}}(f) = \left[Z_{\mathrm{t},1}(f), \ldots, Z_{\mathrm{t},N_{\mathrm{S_t}}}(f)\right]^{\mathrm{T}}$ and $\boldsymbol{Z}_{\mathrm{r}}(f) = \left[Z_{\mathrm{r},1}(f), \ldots, Z_{\mathrm{r},N_{\mathrm{S_r}}}(f)\right]^{\mathrm{T}}$ are the output signal vectors of the scatterers in $\mathcal{R}_{\mathrm{t}}$ and $\mathcal{R}_{\mathrm{r}}$, respectively, with $Z_{\mathrm{t},m}(f)$ denoting the output signal of m-th scatterer $\mathcal{V}_{\mathrm{S_t}}$ and $Z_{\mathrm{r},m}(f)$ denoting the output signal of m-th scatterer $\mathcal{V}_{\mathrm{S_r}}$.

Suppressing the frequency dependency for brevity, we have

$$\boldsymbol{D} = \boldsymbol{0}, \boldsymbol{T} = \begin{bmatrix} \boldsymbol{T}_{\mathrm{t}} \\ \boldsymbol{0} \end{bmatrix}, \boldsymbol{R} = \begin{bmatrix} \boldsymbol{0} & \boldsymbol{R}_{\mathrm{r}} \end{bmatrix}, \boldsymbol{B} = \begin{bmatrix} \boldsymbol{B}_{\mathrm{tt}} & \boldsymbol{B}_{\mathrm{rt}} \\ \boldsymbol{B}_{\mathrm{tr}} & \boldsymbol{B}_{\mathrm{rr}} \end{bmatrix} \tag{1}$$

with sub-matrices containing transfer functions between subsets $\mathcal{V}_{\mathrm{T}}$, $\mathcal{V}_{\mathrm{R}}$, $\mathcal{V}_{\mathrm{S_t}}$, $\mathcal{V}_{\mathrm{S_r}}$ as indicated in the signal flow graph in Fig. 2. $\{\boldsymbol{T}_{\mathrm{t}}, \boldsymbol{R}_{\mathrm{r}}, \boldsymbol{B}_{\mathrm{tt}}, \boldsymbol{B}_{\mathrm{tr}}, \boldsymbol{B}_{\mathrm{rt}}, \boldsymbol{B}_{\mathrm{rr}}\}$ are the transfer functions for edges $\{\mathcal{E}_{\mathrm{Tt}}, \mathcal{E}_{\mathrm{rR}}, \mathcal{E}_{\mathrm{tt}}, \mathcal{E}_{\mathrm{tr}}, \mathcal{E}_{\mathrm{rt}}, \mathcal{E}_{\mathrm{rr}}\}$ denoting the connections between vertices $\{\mathrm{Tx} \to \mathcal{V}_{\mathrm{S_t}}, \mathcal{V}_{\mathrm{S_r}} \to \mathrm{Rx}, \mathcal{V}_{\mathrm{S_t}} \to \mathcal{V}_{\mathrm{S_t}}, \mathcal{V}_{\mathrm{S_t}} \to \mathcal{V}_{\mathrm{S_r}}, \mathcal{V}_{\mathrm{S_r}} \to \mathcal{V}_{\mathrm{S_t}}, \mathcal{V}_{\mathrm{S_r}} \to \mathcal{V}_{\mathrm{S_r}}\}$, respectively. It can be seen that $\boldsymbol{B}$ has non-zero diagonal elements so that the PG model is applicable to scenario with double-directional radio propagation between rooms. In other words, the model

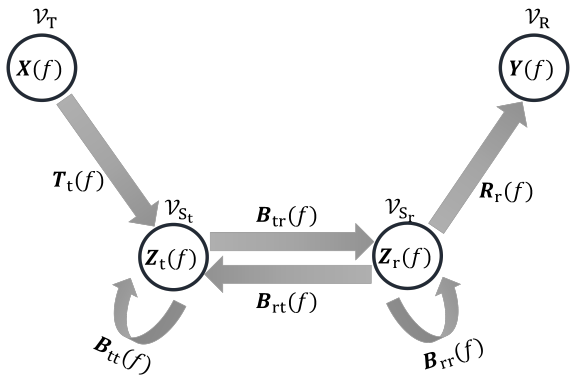

Fig. 2. Schematic diagram for the vector signal flow representing the PG for room-to-room scenario

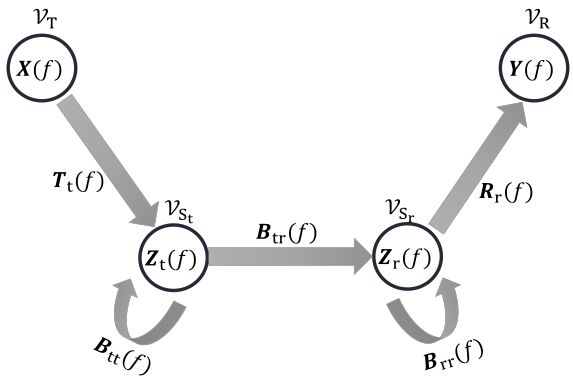

Fig. 3. Vector signal flow graph representing the simplified PG for room-to-room scenario, assuming no propagation from $\mathcal{R}_{\mathrm{r}}$ to $\mathcal{R}_{\mathrm{t}}$

is applicable not only when radio waves transmit from $\mathcal{R}_{\mathrm{t}}$ to $\mathcal{R}_{\mathrm{r}}$; but also when radio waves transmit from $\mathcal{R}_{\mathrm{t}}$ to $\mathcal{R}_{\mathrm{r}}$, then from $\mathcal{R}_{\mathrm{r}}$ to $\mathcal{R}_{\mathrm{t}}$, then again $\mathcal{R}_{\mathrm{t}}$ to $\mathcal{R}_{\mathrm{r}}$.

The channel transfer matrix of the propagation graph reads [9]

$$\boldsymbol{H}_{\mathrm{PG}} = \boldsymbol{D} + \boldsymbol{R}\left[\boldsymbol{I} - \boldsymbol{B}\right]^{-1}\boldsymbol{T}. \tag{2}$$

In (2), the summation of the k-bounce (excluding LOS) propagation paths $\sum_{k=1}^{\infty}\boldsymbol{B}^{k-1}$ converges to $\left[\boldsymbol{I}-\boldsymbol{B}\right]^{-1}$, where the k approaching ∞ indicates the indoor reverberation components. Inserting the above definitions and carrying out the block matrix inversion yield

$$\begin{aligned}\boldsymbol{H}_{\mathrm{PG}} &= \begin{bmatrix} \boldsymbol{0} & \boldsymbol{R}_{\mathrm{r}} \end{bmatrix}\begin{bmatrix} \boldsymbol{I}-\boldsymbol{B}_{\mathrm{tt}} & -\boldsymbol{B}_{\mathrm{rt}} \\ -\boldsymbol{B}_{\mathrm{tr}} & \boldsymbol{I}-\boldsymbol{B}_{\mathrm{rr}} \end{bmatrix}^{-1}\begin{bmatrix} \boldsymbol{T}_{\mathrm{t}} \\ \boldsymbol{0} \end{bmatrix} \\ &= \boldsymbol{R}_{\mathrm{r}}\left\{\boldsymbol{I}-\boldsymbol{B}_{\mathrm{rr}}-\boldsymbol{B}_{\mathrm{tr}}\left[\boldsymbol{I}-\boldsymbol{B}_{\mathrm{tt}}\right]^{-1}\boldsymbol{B}_{\mathrm{rt}}\right\}^{-1} \\ &\quad \boldsymbol{B}_{\mathrm{tr}}\left[\boldsymbol{I}-\boldsymbol{B}_{\mathrm{tt}}\right]^{-1}\boldsymbol{T}_{\mathrm{t}}\end{aligned} \tag{3}$$

where $\boldsymbol{I}$ are the identity matrices of the appropriate dimension. Furthermore, by using binomial inverse theorem, (3) can further be expanded into:

$$\begin{aligned}\boldsymbol{H}_{\mathrm{PG}} &= \boldsymbol{R}_{\mathrm{r}}\left[\boldsymbol{I}-\boldsymbol{B}_{\mathrm{rr}}\right]^{-1}\boldsymbol{B}_{\mathrm{tr}}\left[\boldsymbol{I}-\boldsymbol{B}_{\mathrm{tt}}\right]^{-1}\boldsymbol{T}_{\mathrm{t}} \\ &\quad + \boldsymbol{R}_{\mathrm{r}}\left[\boldsymbol{I}-\boldsymbol{B}_{\mathrm{rr}}\right]^{-1}\boldsymbol{B}_{\mathrm{tr}}\left[\boldsymbol{I}-\boldsymbol{B}_{\mathrm{tt}}\right]^{-1} \\ &\quad \left\{\boldsymbol{I}-\boldsymbol{B}_{\mathrm{rt}}\left[\boldsymbol{I}-\boldsymbol{B}_{\mathrm{rr}}\right]^{-1}\boldsymbol{B}_{\mathrm{tr}}\left[\boldsymbol{I}-\boldsymbol{B}_{\mathrm{tt}}\right]^{-1}\right\}^{-1} \\ &\quad \boldsymbol{B}_{\mathrm{rt}}\left[\boldsymbol{I}-\boldsymbol{B}_{\mathrm{rr}}\right]^{-1}\boldsymbol{B}_{\mathrm{tr}}\left[\boldsymbol{I}-\boldsymbol{B}_{\mathrm{tt}}\right]^{-1}\boldsymbol{T}_{\mathrm{t}}.\end{aligned} \tag{4}$$

In (3) and (4), $\left[\boldsymbol{I}-\boldsymbol{B}_{\mathrm{tt}}\right]^{-1}$ describes the reverberant effect in $\mathcal{R}_{\mathrm{t}}$, $\left[\boldsymbol{I}-\boldsymbol{B}_{\mathrm{rr}}\right]^{-1}$ describes the reverberant effect in $\mathcal{R}_{\mathrm{r}}$, $\boldsymbol{B}_{\mathrm{tr}}$ and $\boldsymbol{B}_{\mathrm{rt}}$ describe the signal flows between rooms. From (3) and (4), it is clear that the reverberant process for room-to-room scenario is caused by an interplay of the reverberation effects in each of the rooms in combination with a reverberation effect due to signal flowing between the rooms. It can also be seen from (4) that the reverberant process is the summation of a simple term representing unidirectional signal flow between rooms and a more complicated term representing bidirectional signal flow between rooms.

Since (3) and (4) are rather involved, it is beneficial to investigate simplifying cases. Here we consider two such cases.

1) Case $\mathcal{R}_{\mathrm{t}} \to \mathcal{R}_{\mathrm{r}}$, no propagation from $\mathcal{R}_{\mathrm{r}}$ to $\mathcal{R}_{\mathrm{t}}$: If there is no propagation from $\mathcal{R}_{\mathrm{r}}$ to $\mathcal{R}_{\mathrm{t}}$, that is, $\boldsymbol{B}_{\mathrm{rt}} = 0$, then (4) simplifies to

$$\boldsymbol{H}_{\mathrm{PG}} = \boldsymbol{R}_{\mathrm{r}}\left[\boldsymbol{I}-\boldsymbol{B}_{\mathrm{rr}}\right]^{-1}\boldsymbol{B}_{\mathrm{tr}}\left[\boldsymbol{I}-\boldsymbol{B}_{\mathrm{tt}}\right]^{-1}\boldsymbol{T}_{\mathrm{t}}. \tag{5}$$

The corresponding vector signal flow is shown in Fig. 3. This structure reflects the fact that there are essentially only two reverberation loops. The numerical examples in later section is based on this assumption, and we show that the simplified PG model is sufficient to predict propagation in the considered environment.

2) Case $\mathcal{R}_{\mathrm{t}} \leftrightarrow \mathcal{R}_{\mathrm{r}}$, assuming 1 time propagation from $\mathcal{R}_{\mathrm{r}}$ to $\mathcal{R}_{\mathrm{t}}$: Please refer to Appendix for the corresponding channel transfer function and vector signal flow graph.

B. Ray Tracing Tool

The 3-D RT tool applied here is based on [21], and can be used to capture propagation mechanisms like LOS, SR, penetration, diffraction and diffuse scattering (DS). This RT tool has been utilized in literature and its effectiveness has been validated, for instance in [18], [22], [23]. The input information are the thorough geometrical and electromagnetic description of the scenario, including walls, ceiling, floor and major furniture, as well as the radiation properties of antennas. Despite the fact that there is no limitation on the reflection order in RT, the highest order is generally set to 3 or 4 to achieve feasible computation time.

C. Hybrid Modeling Algorithm

We propose a hybrid model consisting of a combination of RT and PG. In the model, the PG is obtained by Algorithm 1 based on the Case $\mathcal{R}_{\mathrm{t}} \to \mathcal{R}_{\mathrm{r}}$. The algorithm applies RT tool separately in each room to acquire PG vertices and applies refraction transmission calculation for obtaining edges connecting two surfaces of the separating wall. When conducting RT tool in each room, we assume pseudo-Rx (in $\mathcal{R}_{\mathrm{t}}$) or

Algorithm 1 Modeling algorithm of room-to-room radio channel by using RT and PG in combination

Input: Geometrical information of scenario, electromagnetical properties of major materials, radiation pattern of antennas

Output: PG edges $\mathcal{E}_{\mathrm{Tt}}$, $\mathcal{E}_{\mathrm{tt}}$, $\mathcal{E}_{\mathrm{tr}}$, $\mathcal{E}_{\mathrm{rt}}$, $\mathcal{E}_{\mathrm{rr}}$, $\mathcal{E}_{\mathrm{rR}}$

▷ **Step 1** denote the surface of the separating wall between two rooms in $\mathcal{R}_{\mathrm{t}}$ as $S_{\mathcal{R}_{\mathrm{t}}}$, denote the surface in $\mathcal{R}_{\mathrm{r}}$ as $S_{\mathcal{R}_{\mathrm{r}}}$, divide $S_{\mathcal{R}_{\mathrm{t}}}$ into uniform small tiles with area size ΔS, and find the visible (not blocked) tiles seen from Tx

▷ **Step 2** apply RT tool in $\mathcal{R}_{\mathrm{t}}$ to find the pseudo-LOS and the SR paths between Tx and each visible tile, assuming Rx virtually locates at the center of the tile

▷ **Step 3** conduct transmission check according to Snell's law to see if all paths collected in **Step 2** can reach on $S_{\mathcal{R}_{\mathrm{r}}}$, and delete those paths that can not reach

▷ **Step 4** record the interactive points of the remaining paths in **Step 3** as well as the corresponding pseudo-Rx locations as the vertices in set $\mathcal{V}_{\mathrm{S_t}}$

▷ **Step 5** check each transmitted path coming from $\mathcal{R}_{\mathrm{t}}$ in **Step 3** to see whether the location it arrives on $S_{\mathcal{R}_{\mathrm{r}}}$ is blocked seen from Rx

▷ **Step 6** for those not blocked in **Step 5**, apply RT tool in $\mathcal{R}_{\mathrm{r}}$ to find the pseudo-LOS and the SR paths between each arrival location on $S_{\mathcal{R}_{\mathrm{r}}}$ (assuming Tx virtually locates here) and the Rx

▷ **Step 7** record the interactive points of the paths in **Step 6** as well as the corresponding pseudo-Tx locations on $S_{\mathcal{R}_{\mathrm{r}}}$ as the vertices in set $\mathcal{V}_{\mathrm{S_r}}$

▷ **Step 8** generate edges:

- $\mathcal{E}_{\mathrm{Tt}}$ by connecting Tx to the first interactive points in $\mathcal{V}_{\mathrm{S_t}}$;
- $\mathcal{E}_{\mathrm{tt}}$ by connecting the last interactive points to the corresponding pseudo-Rx locations on $S_{\mathcal{R}_{\mathrm{t}}}$ in $\mathcal{V}_{\mathrm{S_t}}$;
- $\mathcal{E}_{\mathrm{tr}}$ by connecting the pseudo-Rx locations on $S_{\mathcal{R}_{\mathrm{t}}}$ in $\mathcal{V}_{\mathrm{S_t}}$ to the pseudo-Tx locations on $S_{\mathcal{R}_{\mathrm{r}}}$ in $\mathcal{V}_{\mathrm{S_r}}$;
- $\mathcal{E}_{\mathrm{rt}}$ does not exist following (5);
- $\mathcal{E}_{\mathrm{rr}}$ by connecting the pseudo-Tx location on $S_{\mathcal{R}_{\mathrm{r}}}$ to the first interactive points in $\mathcal{V}_{\mathrm{S_r}}$;
- $\mathcal{E}_{\mathrm{rR}}$ by connecting the last interactive points in $\mathcal{V}_{\mathrm{S_r}}$ to Rx.

pseudo-Tx (in $\mathcal{R}_{\mathrm{r}}$) virtually locating on the surface of the separating wall. Through the algorithm, full sets of PG edges can be obtained for the room-to-room scenario.

For the Step 8 of the algorithm, as shown in Fig. 4, the first and the last interactive points for a 1st order SR path are the same, for a 2nd (or higher) order SR path are different. [18] The edges connecting the first to the last interactive points are omitted in the algorithm, and we only focus on the edges connecting Tx (or pseudo-Tx) to the first interactive points and edges connecting the last interactive points to Rx (or pseudo-Rx), because those edges characterize the main features of the directional power spectra seen from Tx (or pseudo-Tx) and Rx (or pseudo-Rx). In addition, for a direct path in $\mathcal{R}_{\mathrm{t}}$ connecting Tx to pseudo-Rx, only the first interactive point is recorded in RT, therefore $\mathcal{E}_{\mathrm{tt}}$ is empty. For a direct path in $\mathcal{R}_{\mathrm{r}}$ connecting

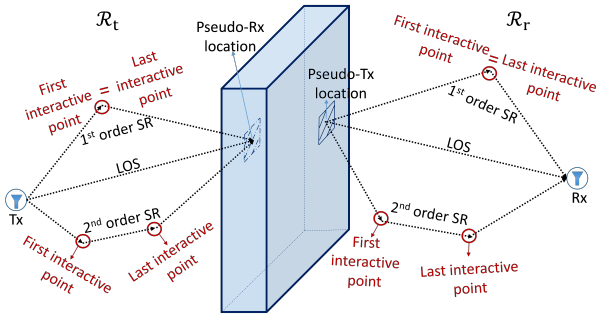

Fig. 4. Illustration of the interaction points obtained from RT that is separately applied in two rooms

pseudo-Tx to Rx, only the last interactive point is recorded in RT, therefore $\mathcal{E}_{\mathrm{rr}}$ is empty. Those pseudo-Rx and pseudo-Tx locations are counted as the vertices in $\mathcal{V}_{\mathrm{S_t}}$ and in $\mathcal{V}_{\mathrm{S_r}}$ respectively.

D. Edge Transfer Function

The edge transfer function [18] is defined as:

$$A_e(f) = \begin{cases} g_e(f)\exp\left(-j2\pi\tau_e f\right) & e \in \mathcal{E} \\ 0 & e \notin \mathcal{E} \end{cases} \tag{6}$$

where $g_e(f)$ is the edge gain, and τ_e is the edge delay. The gains for different edges are defined in Table I, where

$$\begin{aligned} \mu\left(\mathcal{E}'\right) &= \frac{1}{|\mathcal{E}'|}\sum_{e\in\mathcal{E}'}\tau_e, \\ S(\mathcal{E}') &= \sum_{e\in\mathcal{E}'}\tau_e^{-2}, \end{aligned} \tag{7}$$

for any $\mathcal{E}' \subseteq \mathcal{E}$. $|\mathcal{E}'|$ indicates the cardinality. $\mathrm{odi}(e)$ is the out-degree of initial vertex of edge e. The two reverberation time $T_{\mathrm{rev}}^{\mathcal{R}_{\mathrm{t}}}(f)$ and $T_{\mathrm{rev}}^{\mathcal{R}_{\mathrm{r}}}(f)$ of $\mathcal{R}_{\mathrm{t}}$ and $\mathcal{R}_{\mathrm{r}}$, respectively, are defined by Eyring's model [24]:

$$T_{\mathrm{rev}}^{\mathcal{R}_{\mathrm{t}}}(f) = \frac{-4V_{\mathcal{R}_{\mathrm{t}}}}{cS_{\mathcal{R}_{\mathrm{t}}}\ln\left(1-\bar{a}_{\mathcal{R}_{\mathrm{t}}}(f)\right)} \tag{8}$$

$$T_{\mathrm{rev}}^{\mathcal{R}_{\mathrm{r}}}(f) = \frac{-4V_{\mathcal{R}_{\mathrm{r}}}}{cS_{\mathcal{R}_{\mathrm{r}}}\ln\left(1-\bar{a}_{\mathcal{R}_{\mathrm{r}}}(f)\right)} \tag{9}$$

where $V_{\mathcal{R}_{\mathrm{t}}}$ and $V_{\mathcal{R}_{\mathrm{r}}}$ are the room volumes, c is the speed of light, $S_{\mathcal{R}_{\mathrm{t}}}$ and $S_{\mathcal{R}_{\mathrm{r}}}$ are the total surface areas of rooms, $\bar{a}_{\mathcal{R}_{\mathrm{t}}}(f)$ and $\bar{a}_{\mathcal{R}_{\mathrm{r}}}(f)$ are the average room absorption coefficients which are frequency dependent due to electromagnetic properties of the involved materials. Note that the definition of the reverberation time when Tx and Rx are in adjacent rooms from Aliou's measurement observations [19] is for the characterization of the PDP slope of whole channel. But here in (9), the definition of $T_{\mathrm{rev}}^{\mathcal{R}_{\mathrm{r}}}(f)$ is the same as $T_{\mathrm{rev}}^{\mathcal{R}_{\mathrm{t}}}(f)$ due to the design of the proposed algorithm that RT tool is applied separately for each room. γ denotes the ratio between the decay of radio wave propagation inside wall and that in the air. In the case where signals are back and forth through the wall for multiple times,

TABLE I. EDGE DEFINITION

Edge type	Edge gain, g_e	Sub-matrix
$\mathcal{E}_{\mathrm{Tt}}$	$\sqrt{\frac{1}{4\pi f \mu(\mathcal{E}_{\mathrm{Tt}})}\frac{\tau_e^{-2}}{S(\mathcal{E}_{\mathrm{Tt}})}}$	$\boldsymbol{T}_{\mathrm{t}}$
$\mathcal{E}_{\mathrm{rR}}$	$\sqrt{\frac{1}{4\pi f \mu(\mathcal{E}_{\mathrm{rR}})}\frac{\tau_e^{-2}}{S(\mathcal{E}_{\mathrm{rR}})}}$	$\boldsymbol{R}_{\mathrm{r}}$
$\mathcal{E}_{\mathrm{tt}}$	$\sqrt{\frac{\exp(\frac{-\mu(\mathcal{E}_{\mathrm{tt}})}{\mathcal{R}_{\mathrm{t}}})}{\frac{T_{\mathrm{rev}}(f)}{\mathrm{odi}(e)}}}$	$\boldsymbol{B}_{\mathrm{tt}}$
$\mathcal{E}_{\mathrm{rr}}$	$\sqrt{\frac{\exp(\frac{-\mu(\mathcal{E}_{\mathrm{rr}})}{\mathcal{R}_{\mathrm{r}}})}{\frac{T_{\mathrm{rev}}(f)}{\mathrm{odi}(e)}}}$	$\boldsymbol{B}_{\mathrm{rr}}$
$\mathcal{E}_{\mathrm{tr}}$	$\gamma\sqrt{\frac{1}{4\pi f \mu(\mathcal{E}_{\mathrm{tr}})}\frac{\tau_e^{-2}}{S(\mathcal{E}_{\mathrm{tr}})}}$	$\boldsymbol{B}_{\mathrm{tr}}$
$\mathcal{E}_{\mathrm{rt}}$	0	$\boldsymbol{B}_{\mathrm{rt}}$

multiple orders of γ, i.e. γ, γ^3, γ^5, $\cdots$, will effect the final transfer function in (4). Given that the signals experiencing more than two times penetration will be weaker than that experiencing once, the contribution of higher order part of γ can be ignored. In this case, or in the case where signals are assumed to propagate through the wall once, since the gains of all edges reaching at Rx in adjacent room are multiplied with γ, the effect of γ can be removed if power normalization is applied to channel. Therefore, γ can be simply set to 1, and it does not influence the generated channel properties.

III. MEASUREMENT CAMPAIGN

The room-to-room radio channel measurements were carried out at the Maxwell building in Université Catholique de Louvain, Louvain-la-Neuve, Belgium, in the autumn of 2014. The investigated environment was located on the second floor, and consisted of two adjacent typical office rooms separated by a brick wall, as shown on the floor plan in Fig. 5. Both rooms have floor-to-ceiling height of 2.64 m. The two surfaces of the separating brick wall are shown in Fig. 6. Note that part of the wall is the wooden cavity, and the thickness is about 0.65 m. During each measurement, the receive antenna was moved at random by the operator within a horizontal circular area, so that we can average the channels over snapshots to minimize the influences of the operator and the loading stick. These areas are indicated by circles with centroids given as in Fig. 5. [25] The measurements were conducted using UCL/ULB Elektrobit PROPSound$^{\mathrm{TM}}$ Channel Sounder at a carrier frequency of 3.8 GHz. The nodes were connected with the channel sounder using long low-loss RF cables of equal length. These cables have excellent RF stability, even when they are slightly bent or moved during the measurements. At the nodes, custom-made dipole antennas with a gain of 1.75 dB and an omnidirectional radiation pattern were used [26]. The channel sounder used long pseudo-noise sequences to estimate the impulse response of the radio channel between Tx and Rx nodes. The measurement parameters are summarized in Table II.

Among the measured channel impulse responses (CIR) for all snapshots (time samples), there may exist some snapshots that have significantly different power compared to the rest due to the mechanical vibrations or the occasional switching error. Outlier filtering [27] is implemented to eliminate the bad snapshots. For each Rx location, the measured CIR are averaged over all good snapshots to reflect the **average PDP trend** at around the Rx position. The average PDP shows the main features of the CIR at each position ignoring any small scale fading.

TABLE II. MEASUREMENT PARAMETERS AFTER POST-PROCESSING

Parameter	Value
Center frequency	3.8 GHz
Transmit power	23 dBm
Measurement bandwidth	200 MHz
Recorded delay chips C	2048
Recorded time samples N_s	6000
Measurement duration	60 s
Code length	20.47 μs

TABLE III. MATERIAL PROPERTIES AT AROUND 3.8 GHZ USED IN RT

	Brick wall	Wood	Glass	Floor/Ceiling	Metal
Permittivity	4.47	2.01	4.60	7.15	100
Conductivity [S/m]	0.01	0.002	0	0.004	0
Refractive index	1.8	1.5			

IV. VALIDATION

To validate the proposed model, its predictions of the CIR of room-to-room channels are compared with the measured data. Furthermore, the proposed hybrid model is also compared with the conventional RT tool. It is worth noting that the hamming window is multiplied with the predicted channel transfer functions when conducting inverse Fourier transform to obtain CIR.

The electromagnetic properties of materials at around 3.8 GHz [23], [28], [29] shown in Table III are imported to RT. No scattering from ground is considered and ground is not penetrable.

The simplest PG assuming no propagation from $\mathcal{R}_{\mathrm{r}}$ to $\mathcal{R}_{\mathrm{t}}$ is used in the proposed model. The resulting CIR is denoted as h^m_{prop} for the Rx location m, and is compared to the measured h^m_{mea}. Since 1) the measurement addressed the average PDP as the most important parameter, and 2) the simulated channel is instantaneous, the PDP discrepancy between the predicted and the measured channels is defined by the relative error as follows:

$$\xi^m = \frac{\left|\sum_\tau \mathrm{PDP}^m_{\mathrm{prop}}(\tau) - \mathrm{PDP}^m_{\mathrm{mea}}(\tau)\right|}{\sum_\tau \left|\mathrm{PDP}^m_{\mathrm{mea}}(\tau)\right|} \tag{10}$$

where

$$\mathrm{PDP}^m_{\mathrm{prop}}(\tau) = 20\log_{10}\left|h^m_{\mathrm{prop}}(\tau)\right| \tag{11}$$

is the predicted instantaneous PDP,

$$\mathrm{PDP}^m_{\mathrm{mea}}(\tau) = 20\log_{10}\overline{\left|h^m_{\mathrm{mea}}(\tau)\right|} \tag{12}$$

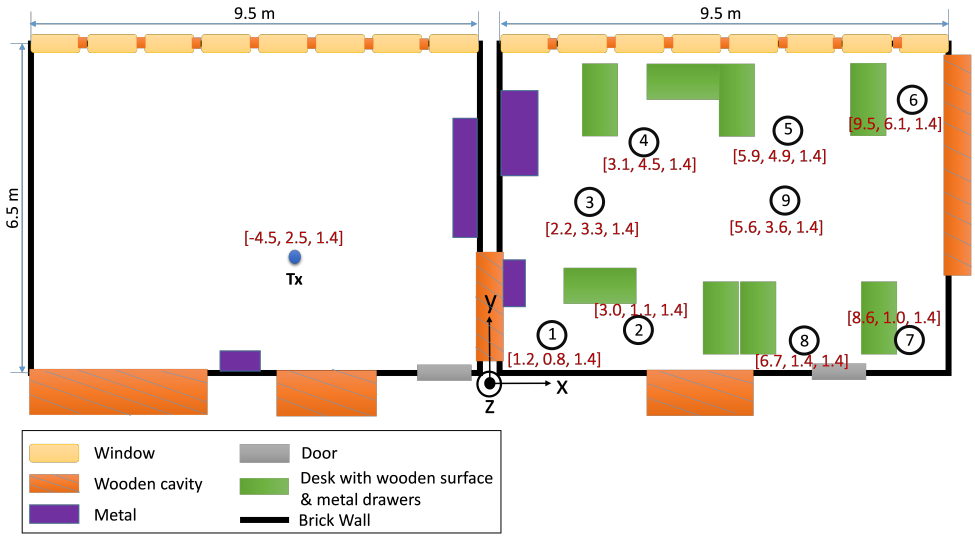

Fig. 5. Measurement scenario

Fig. 6. The separating wall in room-to-room measurement: (a) in $\mathcal{R}_t$ (b) in $\mathcal{R}_r$

is defined by the envelope-averaged measured PDP over all snapshots, and τ is the delay. Both of the PDPs are normalized to the maximum power of delay bins.

What matters the most for a predicted CIR is the part from the first power peak until the power convergence (the beginning of noise floor, or the end of the reverberant slope), as is demonstrated in Fig. 7. Therefore, the discrepancy check focuses on whether the predicted CIR can reflect the major multipaths and the reverberant slope of the measured reference.

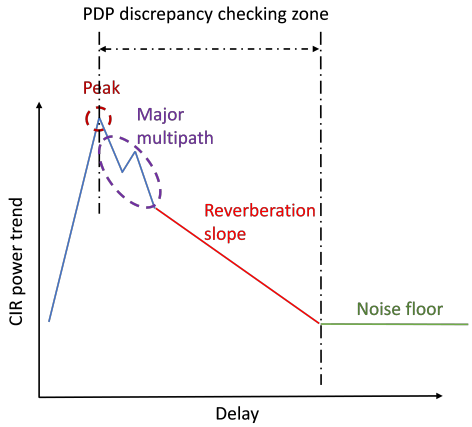

Fig. 7. Demonstration for the PDP trend consisting of peak, major multipaths, reverberation slope and noise floor

The evaluations do not only focus on the relative error of the whole PDP, but also separately on the major multipath components and the reverberation slope.

A. Numerical Results

To start with, we mimic the measurement process by simulating the channels on a circle whose radius is 0.6 m and is centered at the Rx location marked in Fig. 5. Fig. 8 (a) shows the predicted CIR PDP for 10 locations uniformly spaced on the circle centered at Rx position No.2 as well as the average PDP over all those 10 locations. Here the tile size ΔS and the SR order in the proposed modeling are 0.04^2 m^2 (0.04 is approximately the half wavelength at central frequency) and 1, respectively. For comparison, Fig. 8 (b) shows the measured PDP of each snapshot as well as the average over all snapshots. For a fair comparison, we randomly choose 10 snapshots along

with the average of these and show in Fig. 8 (c). All PDPs are normalized to the peak of the average PDP. It is apparent from Fig. 8 that both the predicted and measured PDPs are sensitive to Rx locations. In comparison, the spatially averaged PDPs are much smoother. The measurement technique does not give exact information on the Rx position for each snapshot. This prevents direct comparison of the PDPs at particular positions. However, in the following contents, we investigate prediction of the PDP assuming the Rx positions to be at the center of the circle which are marked in Fig. 5. We compare the predicted PDP by proposed model to the spatially averaged PDP of the measured data.

To apply the proposed model, proper settings of the tile size parameter ΔS and the SR order are needed. We now investigate how the model is affected by the settings of the tile size parameter ΔS and the SR order. For this purpose, we consider the Rx position No.2 and vary the parameters according to Table IV. Fig. 9 and Fig. 10 shows the comparisons of the CIR PDPs when SR order is 1 and 2 respectively, and ΔS is

(a) about 0.04^2 m^2 ($0.04 \approx 0.5\lambda_c$ where λ_c is the carrier wavelength), totally 162×66 tiles on $S_{\mathcal{R}_t}$;
(b) about 0.08^2 m^2 ($0.08 \approx \lambda_c$), totally 81×33 tiles;
(c) about 0.12^2 m^2 ($0.12 \approx 1.5\lambda_c$), totally 54×22 tiles;
(d) about 0.16^2 m^2 ($0.16 \approx 2\lambda_c$), totally 41×17 tiles on $S_{\mathcal{R}_t}$;
(e) about 0.20^2 m^2 ($0.20 \approx 2.5\lambda_c$), totally 33×13 tiles;
(f) about 0.24^2 m^2 ($0.24 \approx 3\lambda_c$), totally 27×11 tiles.

Visual inspections of Fig. 9 and Fig. 10 along with prediction performances of the mean delay and rms delay spread indicate that: the model's predictions of mean delay and rms delay spread are sensitive to the choice of ΔS and SR interaction order. It is clear from the figures that the tile size does affect the prediction of PDP slopes. This effect is also reflected in the relative PDP error in Table IV, where ξ_{MP}, ξ_{SL}, and ξ are the relative errors for major multipath components from 35 ns to 100 ns, for reverberation slope from 100 ns to 250 ns, and for multipath components (from the first peak until the beginning of convergence to noise floor) from 35 ns to 250 ns, respectively. However, there is no obvious trend of the performance with the increase of the tile size. This is because that the interactive points for building PG in $\mathcal{R}_t$ are collected by applying RT in this room and assuming that the Rx virtually locates at the center of each tile on the surface of the separating wall. The increase of tile size does not necessarily result in less sufficient collection of interactive points, since the goodness of the interactive points totally depends on the locations of the pseudo-Rx but not the density. Nevertheless, according to the sampling theorem, half the wavelength is the safest choice for the tile size.

The SR order of the RT tool also affect the performance of the proposed model. The RT tool is applied separately for the adjacent rooms; for reasons of simplicity, we assume that the SR orders in RT are the same for both rooms. Comparing the results in Fig. 9 when SR order is 1 with Fig. 10 when SR order is 2, we observe that a higher SR order does not necessarily lead to a significant improvement in predicting the PDP for our algorithm. This observation is also reflected in the relative PDP errors given in Table IV. The reasons could

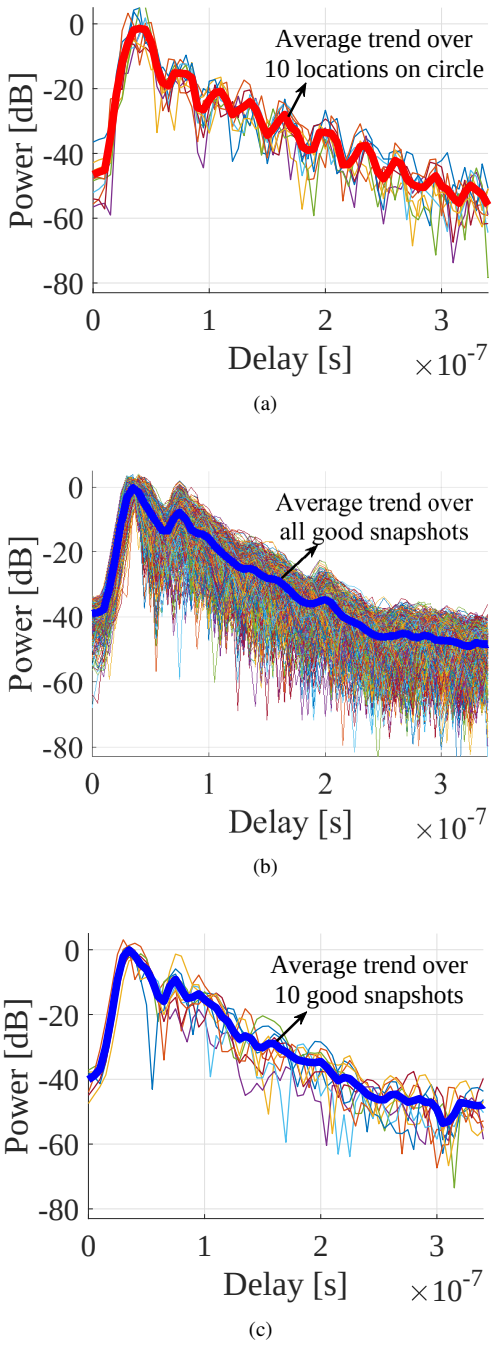

Fig. 8. Numerical example for Rx position No.2: (a) simulated CIR PDP by proposed approach where Rx is on the circle centered at marked position in Fig. 5 (b) measured CIR PDP of each snapshot and the average PDP trend over all good snapshots (c) measured CIR PDP of random 10 good snapshots and the average PDP over these 10 snapshots

be as follows. In fact, the average power level of the second order SR paths from $\mathcal{R}_t$ is already lower than that of the first order SR paths. When they propagates in $\mathcal{R}_r$, the power level arriving at Rx maybe very low and can be neglected. But in our

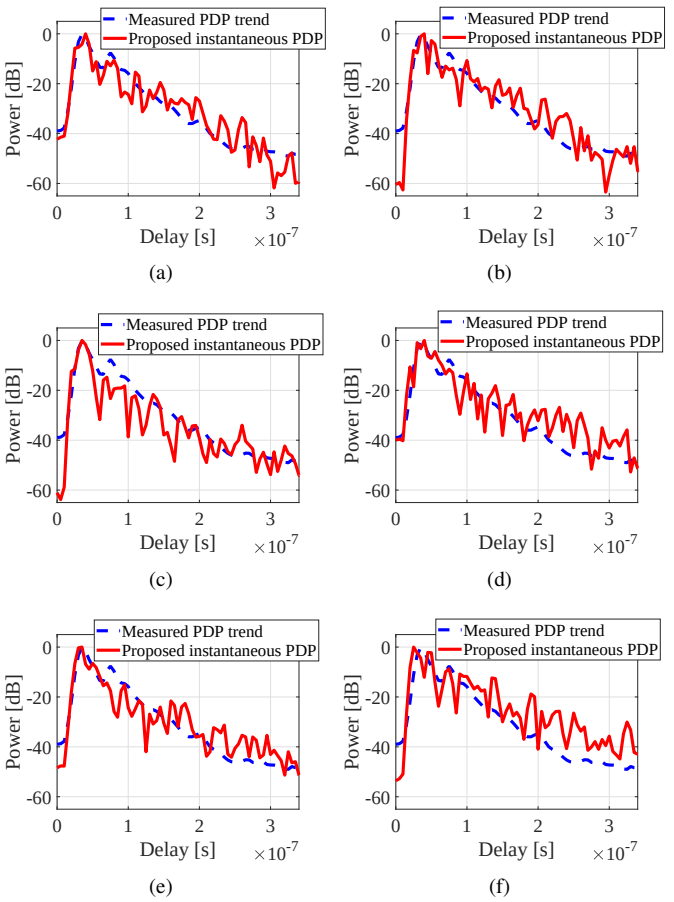

Fig. 9. Numerical examples for Rx location 2 with different settings in proposed hybrid modeling: (a) scenario index a_1 (b) scenario index b_1 (c) scenario index c_1 (d) scenario index d_1 (e) scenario index e_1 (f) scenario index f_1

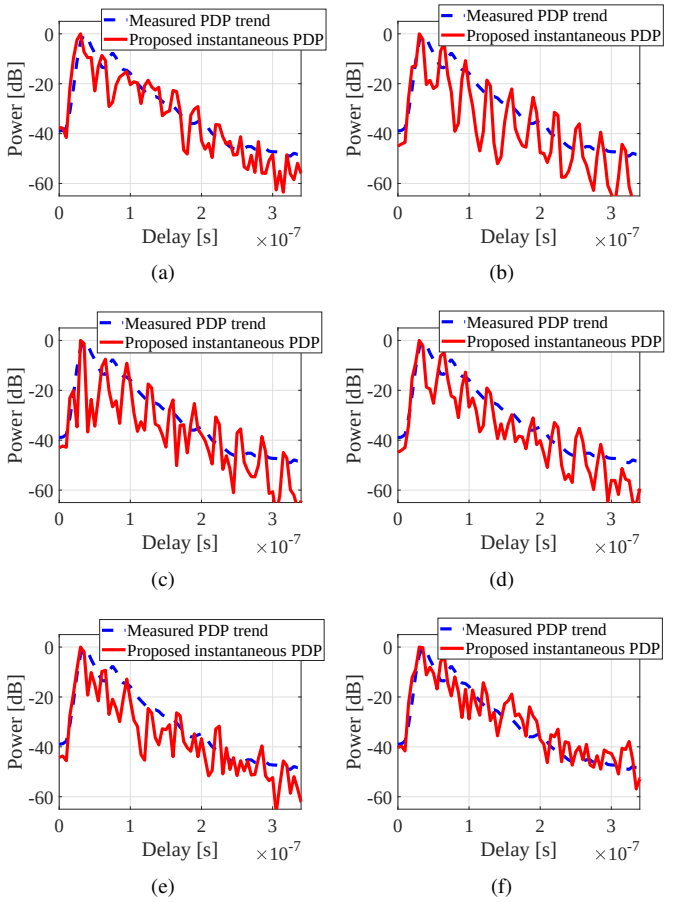

Fig. 10. Numerical examples for Rx location 2 with different settings in proposed hybrid modeling: (a) scenario index a_2 (b) scenario index b_2 (c) scenario index c_2 (d) scenario index d_2 (e) scenario index e_2 (f) scenario index f_2

algorithm, since RT tool is separately applied at each room, using SR order of 2 in $\mathcal{R}_{\mathrm{r}}$ may exaggerate the second order SR paths coming from $\mathcal{R}_{\mathrm{t}}$. Despite the fact that increasing SR order may not lead to a better prediction of room-to-room radio channel, the SR setting, however, does have a large impact on the runtime of the algorithm. Increasing the SR order from 1 to 2 increases the computation time from less than 780 s to more than 1220 s. For this reason, we propose to set the SR order to 1. Here the runtime is obtained by using the same computer with Intel(R) Core(TM) $\mathrm{i5}-4690$ CPU and refers to the time consumption for PG vertices acquisition in proposed model.

In addition, we evaluate the performance of the proposed hybrid modeling using RT and PG by comparing with the result using simply the conventional RT tool where only the two rooms are considered and we assume that no transmission occur through the other walls than the wall separating the two rooms. For the case using simply the RT tool, not only SR, but also the diffraction, penetration, and DS are involved. The DS mechanism is modeled by the Directive effective roughness model [30] with the scattering parameter set as 0.4 and the integer indicating the width of the scattering lobe set as 4. We consider three scenarios when using RT-only:

(1) 1st order SR + Diffraction + DS (single bounce) + Penetration;
(2) 2nd order SR + Diffraction + DS (single bounce + scattering before and after reflection) + Penetration;
(3) 3rd order SR + Diffraction + DS (single bounce + scattering before and after reflection) + Penetration.

RT is only implemented once at the center frequency. Fig. 11 shows the resulting PDPs for Rx location No.2. Table V shows the PDP discrepancy, the mean delay and the r.m.s delay spread of the resulting h_{RT} by using simply the conventional RT tool. The time consumption for calculating one radio channel using simply RT in case (1), case (2) and case (3) are shown in the table. For comparison, the time consumption for PG vertices acquisition in proposed modeling with settings $\Delta S \approx 0.04^2$ m^2 and SR order 1, Fig. 9 (a), is about 780 s. Despite the fact that Fig. 11 (b) and (c) predicts the power trend of the major multipath components not so bad, the predictions of the reverberation slope are much worse than the proposed model

TABLE IV. PERFORMANCE OF PROPOSED MODELING WITH DIFFERENT PARAMETER SETTINGS FOR RX LOCATION NO.2

Index		ΔS	SR order	Run time [s]	ξ_{MP} %	ξ_{SL} %	ξ %	Mean delay [μs]	r.m.s. delay spread [μs]
	h_{mea}							1.33	0.70
a_1	h_{prop}	0.04	1	771	4.9	7.2	2.3	1.35	0.65
b_1	h_{prop}	0.08		323	2.7	12.8	10.1	1.39	0.69
c_1	h_{prop}	0.12		158	9.3	8.9	18.2	1.37	0.69
d_1	h_{prop}	0.16		87	2.3	9.5	7.2	1.34	0.66
e_1	h_{prop}	0.20		75	5.7	3.6	2.1	1.39	0.67
f_1	h_{prop}	0.24		53	2.9	20.2	17.3	1.39	0.66
a_2	h_{prop}	0.04	2	14561	8.1	1.9	9.9	1.31	0.67
b_2	h_{prop}	0.08		7218	10.9	18.9	29.8	1.29	0.68
c_2	h_{prop}	0.12		3449	13.1	10.8	23.9	1.31	0.68
d_2	h_{prop}	0.16		2012	9.3	13.1	22.4	1.29	0.67
e_2	h_{prop}	0.20		1669	9.5	14.4	23.9	1.32	0.68
f_2	h_{prop}	0.24		1223	5.0	6.0	1	1.32	0.66

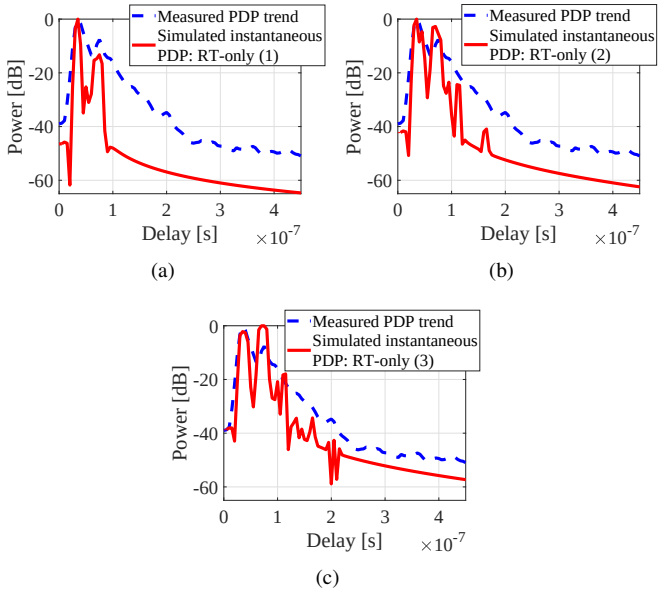

Fig. 11. Numerical examples for Rx location 2, when using only RT and involving whole mechanisms (a) SR (1st order), diffraction, DS, penetration (b) SR (2nd order), diffraction, DS, penetration (c) SR (3rd order), diffraction, DS, penetration

and it takes more than twice the time comparing with the proposed modeling with settings $\Delta S \approx 0.04^2$ m^2 and SR order 1. Moreover, the predicted instantaneous channel by using simply the conventional RT seems lack of sufficient multipath except for the major peaks, that is why the slopes in Fig. 11 look less turbulent than the results by proposed modeling.

Finally, we compare the performance of the proposed model to the conventional RT tool in terms of accuracy and computation time. Here we consider all the Rx locations. For the proposed model, we use $\Delta S \approx 0.04^2$ m^2 and SR order 1.

TABLE V. PERFORMANCE OF RT-ONLY FOR RX LOCATION NO.2

	Run time [s]	ξ_{MP} %	ξ_{SL} %	ξ %	Mean delay [μs]	r.m.s. delay spread [μs]
h_{mea}					1.33	0.70
$h_{\mathrm{RT}(1)}$	68	21.1%	58.5%	79.6%	1.32	0.69
$h_{\mathrm{RT}(2)}$	1545	6.1%	40.8%	47.0%	1.30	0.67
$h_{\mathrm{RT}(3)}$	1610	3.8%	25.4%	29.2%	1.30	0.66

For the conventional RT tool, we set the SR order to 3 and include SR, diffraction, DS and penetration. Table VI reports the relative PDP error, the computation time, the mean delay, and the r.m.s. delay spread for each Rx location. In the table, the delay ranges to calculate ξ_{MP}, ξ_{SL} and ξ are adjusted for each Rx location.

Comparing the averages given in Table VI, we find that overall both methods predict with good accuracy the mean delay and the rms delay spread with some small variations. Interestingly, the measured mean delays vary about 20 ns for different Rx locations, and the variations happen at positions which are closer to the separating wall. This variations could be a result of a reverberation effect in room $\mathcal{R}_{\mathrm{r}}$. At positions nearby the separating wall, the early signal components due to transmission are stronger than the sum of the reverberation components; further into the room, the diffuse signal due to reverberation dominates the received power and thus the mean delay are stable. This effect is similar to the reverberation phenomenon studied via the reverberation distance in [31] for the single-room scenario.

The average relative PDP error is smaller for the proposed model, particularly in the reverberation slope. This better performance of the proposed model is due to the infinite loop of the gain calculation for the diffuse tail of reverberation. It also appears from the table, that the performance of the proposed modeling is relatively more stable than the conventional RT tool in terms of the PDP discrepancy. While the former ranges from 2.3% to 19.2%, the latter ranges from 22.3% to 89.1%, which indicates that the conventional RT tool is very sensitive to the particular Rx position.

The required computation times differ significantly: the average computation time of the proposed model is about halved compared to the conventional RT. This results from replacing a single RT with high interaction order (here 3) to two separate RT with low interaction order (here 1) plus the computation of the propagation graph. Thus overall, the proposed model gives a significant improvement in prediction accuracy and a significant reduction in computation time for all locations.

V. CONCLUSION

In this paper, we proposed a hybrid model which combines ray tracing and propagation graph to predict the power delay profile of the room-to-room radio propagation channel. By comparison to measured data from a real-world scenario, we find that the proposed model is able to predict the major multipath components and the slope of the reverberation tail

TABLE VI. PERFORMANCE OF PROPOSED MODELING WITH SR ORDER 1 AND ΔS EQUALS 0.04^2 M^2 FOR ALL RX LOCATIONS

Rx location	Computation time [s]		$\xi_{\{\mathrm{prop,mea}\}}$			$\xi_{\{\mathrm{RT(3),mea}\}}$			Mean delay [μs]			r.m.s. delay spread [μs]		
index	h_{prop}	$h_{\mathrm{RT(3)}}$	ξ_{MP}	ξ_{SL}	ξ	ξ_{MP}	ξ_{SL}	ξ	h_{prop}	h_{mea}	$h_{\mathrm{RT(3)}}$	h_{prop}	h_{mea}	$h_{\mathrm{RT(3)}}$
1	778	1728	5.4%	8.4%	3.5%	1.6%	23.9%	22.3%	1.33	1.33	1.36	0.68	0.71	0.69
2	782	1610	4.9%	7.2%	2.3%	3.8%	25.4%	29.2%	1.35	1.33	1.30	0.65	0.70	0.66
3	819	931	14.2%	11.8%	17.3%	11.4%	87.2%	89.1%	1.33	1.35	1.30	0.66	0.69	0.70
4	851	1211	13.2%	2.8%	13.4%	9.4%	72.7%	82.1%	1.37	1.35	1.27	0.66	0.70	0.70
5	868	1478	5.1%	2.7%	4.8%	9.0%	35.2%	44.2%	1.38	1.34	1.35	0.67	0.70	0.69
6	843	1598	12.4%	7.3%	19.2%	16.5%	50.6%	67.4%	1.39	1.34	1.28	0.68	0.70	0.69
7	786	1647	11.9%	9.5%	13.2%	20.4%	60.5%	81.9%	1.37	1.34	1.29	0.66	0.70	0.69
8	798	1604	15.8%	4.0%	11.8%	9.4%	53.5%	63%	1.37	1.34	1.31	0.67	0.70	0.70
9	897	1454	5.7%	3.9%	5.9%	9.6%	63.8%	79.3%	1.33	1.34	1.32	0.66	0.70	0.71
Average	825	1473	9.8%	6.4%	10.2%	10.1%	52.5%	62.1%	1.36	1.34	1.31	0.67	0.70	0.69

of the room-to-room scenario. Although the proposed model is similarly accurate as the conventional ray tracers (when reflection order is large enough) in predicting the major multipath components, it is much more accurate in predicting the reverberation slope following the major peaks, hence is more accurate in predicting the overall PDP. The proposed model is less computationally demanding than conventional ray tracers to achieve the decent accuracy with relative PDP error smaller than 30%. In the demonstrated examples, setting the conventional ray tracer with SR order up to 3 even achieves less accuracy than setting the proposed model with SR order of 1 at each room, while the computational complexity increases dramatically with the increase of the reflection order.

Our observations confirm other studies on hybrid models which integrate ray tracing and propagation graph approaches. The hybrid model benefits most from the accuracy of the ray tracer for the early and dominant components, while the later parts are adequately represented by a less accurate and less computationally demanding method such as the propagation graph. The results from this approach underline the potential gain from combining models with different strengths and weaknesses.

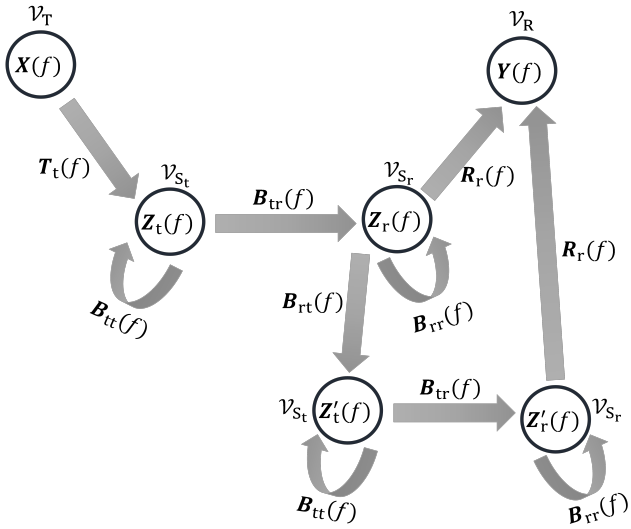

Fig. 12. Schematic diagram for the vector signal flow representing the PG for room-to-room scenario, assuming there is 1 time propagation from $\mathcal{R}_{\mathrm{r}}$ to $\mathcal{R}_{\mathrm{t}}$

APPENDIX

Assuming 1 time propagation from $\mathcal{R}_{\mathrm{r}}$ to $\mathcal{R}_{\mathrm{t}}$, the channel transfer function of PG (4) becomes

$$\begin{aligned}\boldsymbol{H}_{\mathrm{PG}} = &\boldsymbol{R}_{\mathrm{r}}\left[\boldsymbol{I}-\boldsymbol{B}_{\mathrm{rr}}\right]^{-1}\boldsymbol{B}_{\mathrm{tr}}\left[\boldsymbol{I}-\boldsymbol{B}_{\mathrm{tt}}\right]^{-1}\boldsymbol{T}_{\mathrm{t}}\\ &+\boldsymbol{R}_{\mathrm{r}}\left[\boldsymbol{I}-\boldsymbol{B}_{\mathrm{rr}}\right]^{-1}\boldsymbol{B}_{\mathrm{tr}}\left[\boldsymbol{I}-\boldsymbol{B}_{\mathrm{tt}}\right]^{-1}\boldsymbol{B}_{\mathrm{rt}}\left[\boldsymbol{I}-\boldsymbol{B}_{\mathrm{rr}}\right]^{-1}\\ &\boldsymbol{B}_{\mathrm{tr}}\left[\boldsymbol{I}-\boldsymbol{B}_{\mathrm{tt}}\right]^{-1}\boldsymbol{T}_{\mathrm{t}}\end{aligned} \tag{13}$$

and the corresponding vector signal flow is shown in Fig. 12. (13) is obtained by taking the 1st element of Neumann series expanding the loop $\left\{\boldsymbol{I}-\boldsymbol{B}_{\mathrm{rt}}\left[\boldsymbol{I}-\boldsymbol{B}_{\mathrm{rr}}\right]^{-1}\boldsymbol{B}_{\mathrm{tr}}\left[\boldsymbol{I}-\boldsymbol{B}_{\mathrm{tt}}\right]^{-1}\right\}^{-1}$ in (4).

ACKNOWLEDGEMENT

The authors would like to thank Aliou Bamba from Cea Leti, France, for assisting the measurement.

REFERENCES

[1] K. Saito, J.I. Takada, M. Kim, "Dense Multipath Component Characteristics in 11-GHz-Band Indoor Environments," *IEEE Trans. Antennas Propag.,* vol. 65, no. 9, pp. 4780-4789, Sep. 2017.

[2] J. Poutanen, J. Salmi, K. Haneda, V.M. Kolmonen, F. Tufvesson, P. Vainikainen, "Propagation Characteristics of Dense Multipath Components," *IEEE Antennas and Wireless Propagation Letters,* vol. 9, pp. 791-794, Aug. 2010.

[3] A. Richter, J. Salmi, and V. Koivunen, "Distributed Scattering in Radio Channels and Its Contribution to MIMO Channel Capacity," in *Proc. 1st Eur. Conf. Antennas Propag. (EuCAP),* pp.1-7, Nov. 2006.

[4] N. Czink, A. Richter, E. Bonek, J.P. Nuutinen,and J. Ylitalo, "Including Diffuse Multipath Parameters in MIMO Channel Models," in *Proc. 66th IEEE Veh. Technol. Conf. (VTC),* pp. 874-878, Sep. 2007.

[5] M. Landmann, M. Kaeske, R. Thoma, J.I. Takada, and I. Ida, "Measurement Based Parametric Channel Modeling Considering Diffuse Scattering and Specular Components," in *Proc. Int. Symp. Antennas Propag.,* Niigata, Japan, pp. 153-156, Aug. 2007.

[6] J.B. Andersen, J.O. Nielsen, G.F. Pedersen, G. Bauch, and M. Herdin, "Room Electromagnetics," *IEEE Antenna Propag. Magazine*, vol. 49, no. 2, pp. 27-33, 2007.

[7] C.L. Holloway, M.G. Cotton, and P. McKenna, "A Model for Predicting the Power Delay Profile Characteristics Inside a Room," *IEEE Trans. Veh. Technol.,* vol. 48, no. 4, pp. 1110-1120, Jul. 1999.

[8] D.A. Hill, *Electromagnetic Fields in Cavities: Deterministic and Statistical Theories* (IEEE Press Series on Electromagnetic Wave Theory), Piscataway, NJ. USA: Wiley, 2009.

[9] T. Pedersen, G. Steinbock, and B.H. Fleury, "Modeling of Reverberant Radio Channel Using Propagation Graphs," *IEEE Trans. Antennas Propag.*, vol. 60, no. 12, pp. 5978-5988, 2012.

[10] L. Tian, V. Degli-Esposti, E.M. Vitucci, and X. Yin, "Semi-Deterministic Radio Channel Modeling Based on Graph Theory and Ray-Tracing," *IEEE Trans. Antennas Propag.*, vol. 64, no. 6, pp. 2475-2486, 2016.

[11] J. Pascual-Garcia, J.M. Molina-Garcia-Pardo, M.T. Martnez-Ingls, J.V. Rodrguez, and N. Saurn-Serrano, "On the Importance of Diffuse Scattering Model Parameterization in Indoor Wireless Channels at mm-Wave Frequencies," *IEEE Access*, vol. 4, pp. 688?701, Feb. 2016.

[12] V. Degli-Esposti, F. Fuschini, E.M. Vitucci, and G. Falciasecca, "Measurement and modeling of scattering from buildings," *IEEE Trans. Antenna Propag.*, vol. 55, no. 1, Jan. 2007.

[13] E.M. Vitucci, F. Mani, V. Degli-Esposti, and C. Oestges, "Polarimetric Properties of Diffuse Scattering from Building Walls: Experimental Parameterization of a Ray-Tracing Model," *IEEE Trans. Antennas Propag.,* vol. 60, no. 6, pp. 2961-2969, Jun. 2012.

[14] J. Jarvelainen, K. Haneda, M. Kyro, V.M. Kolmonen, J.I. Takada, and H. Hagiwara, "60 GHz Radio Wave Propagation Prediction in a Hospital Environment Using an Accurate Room Structural Model", in *Proc. Loughborough Antennas Propag. Conf. (LAPC)*, Nov. 2012.

[15] T. Pedersen, G. Steinbock, B.H. Fleury, "Modeling of Outdoor-to-Indoor Radio Channels via Propagation Graphs," in *General Assembly and Scientific Symposium (URSI GASS), 2014 XXXIth URSI*, 2014.

[16] R. Zhang, X. Lu, Z. Zhong, L. Cai, "A Study on Spatial-temporal Dynamics Properties of Indoor Wireless Channels," in *International Conference on Wireless Algorithms, Systems, and Applications,* pp. 410-421, 2011.

[17] J. Chen, X. Yin, L. Tian, M.D. Kim, "Millimeter-Wave Channel Modeling Based on A Unified Propagation Graph Theory," *IEEE Communications Letters,* vol. 21, no. 2, Feb. 2017.

[18] G. Steinbock, M. Gan, P. Meissner, E. Leitinger, K. Witrisal, T. Zemen, T. Pedersen, "Hybrid Model for Reverberant Indoor Radio Channels Using Rays and Graphs," *IEEE Trans. Antennas Propag.*, vol. 64, no. 9, pp. 4036-4048, 2016.

[19] A. Bamba, W. Joseph, J.B. Andersen, E. Tanghe, G. Vermeeren, D. Plets, J.O. Nielsen, and L. Martens, "Experimental Assessment of Specific Absorption Rate Using Room Electromagnetics", *IEEE Trans. Electromagnetic Compatibility*, vol. 54, no. 4, pp. 747-757, Aug. 2012.

[20] A. Bamba, W. Joseph, E. Tanghe, G. Vermeeren, and L. Martens, "Circuit Model for Diffuse Multipath and Electromagnetic Absorption Prediction in Rooms," *IEEE Trans. Antennas and Propagation,* vol. 61, no. 6, pp. 3292-3301, Jun. 2013.

[21] F. Mani, "Improved Ray-Tracing for Advanced Radio Propagation Channel Modeling," *Ph.D Thesis of Universite Catholique de Louvain*, Jun. 2012.

[22] F. Mani, F. Quitin, and C. Oestges, "Directional Spreads of Dense Multipath Components in Indoor Environments: Experimental Validation of a Ray-Tracing Approach," *IEEE Trans. Antennas Propag.*, vol. 60, no. 7, pp. 3389-3396, Jul. 2012.

[23] F. Mani, F. Quitin, and C. Oestges, "Accuracy of Depolarization and Delay Spread Predictions Using Advanced Ray-based Modeling in Indoor Scenarios," *EURASIP J. Wireless Commun. Netw.*, vol. 2011, no. 11, Jun. 2011.

[24] G. Steinbock, T. Pedersen, B.H. Fleury, W. Wang, and R. Raulefs, "Experimental Validation of the Reverberation Effect in Room Electromagnetics," *IEEE Trans. Antenna Propag.*, vol. 63, no. 5, May 2015.

[25] E. Vinogradov, "Multi-Dimensional Radio Channel Models for Distributed Communication," *Ph.D Thesis of Universite Catholique de Louvain*, Feb. 2017.

[26] E. Vinogradov, W. Joseph, C. Oestges, "Measurement-based Modeling of Time-Variant Fading Statistics in Indoor Peer-to-Peer Scenarios," *IEEE Trans. Antenna Propag.*, vol. 63, no. 5, May 2015.

[27] V. Kristem, S. Sangodoyin, C.U. Bas, M. Kaske, J. Lee, C. Schneider, G. Sommerkorn, C.J.Z. Zhang, R.S. Thoma, A.F. Molisch, "3D MIMO Outdoor-to-Indoor Propagation Channel Measurement," *IEEE Trans. Wireless Commun.*, vol. 16, no. 7, May 2017.

[28] A. Muqaibel, A. Safaai-Jazi, A. Bayram, A.M. Attiya, and S.M. Riad, "Ultrawideband through-the-wall propagation," in *IEE Proc.-Microw. Antennas Propag.,* vol. 152, no. 6, Dec. 2005.

[29] O. Landron, M.J. Feuerstein, T.S. Rappaport, "A Comparison of Theoretical and Empirical Reflection Coefficients for Typical Exterior Wall Surfaces in a Mobile Radio Environment," *IEEE Trans. Antennas Propag.*, vol. 44, no. 3, Mar. 1996.

[30] V.D. Esposti, F. Fuschini, E.M. Vitucci, and G. Falciasecca, "Measurement and modeling of scattering from buildings," *IEEE Trans. Antenna Propag.*, vol. 55, no. 1, Jan. 2007.

[31] G. Steinbock, T. Pedersen, B.H. Fleury, W. Wang, R. Raulefs, "Distance Dependent Model for the Delay Power Spectrum of In-room Radio Channels," *IEEE Trans. Antenna Propag.*, vol. 61, No. 8, Aug. 2013.

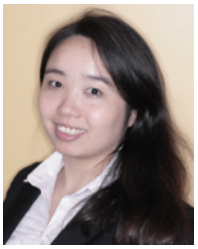

Yang Miao was born in Xinxiang, China, on July 22, 1988. She received the M. Sc. and the Ph.D. degrees from the antenna and radio propagation lab, Department of International Development Engineering, Tokyo Institute of Technology, Japan, in 2012 and 2015, respectively. From October 2010 to September 2015, she was a Research Assistant with Takada Lab, the Mobile Communications Research Group (MCRG), Tokyo Institute of Technology. From October 2015 to January 2018, she was a Postdoctoral Researcher with Institute of Information and Communication Technologies, Electronics and Applied Mathematics (ICTEAM), Université Catholique de Louvain, and with the IMEC/WAVES (Wireless, Acoustics, Environment and Expert Systems) lab, Ghent University, Belgium. She stayed with Jaguar Radio Wave Corporation, Shenzhen, China, from October 2017 to March 2018, as a part-time Senior Antenna Engineer. From April 2018, she became a Research Assistant Professor in Department of Electrical and Electronic Engineering, Southern University of Science and Technology, Shenzhen, China. Dr. Miao's scientific work is focused on the interaction between antenna arrays and physical radio propagation environment. Her research work dealt with spherical antenna measurement, array radiation pattern reconstruction in spatial and frequency domains, indoor radio channel measurement, antenna-channel interaction, antenna de-embedding and channel modeling in both plane wave and spherical vector wave domains, diffuse scattering correlation for radio propagation prediction, reverberation channel prediction using hybrid methods of ray tracing and propagation graph, human detection and positioning using indoor radio channel properties, over-the-air testing emulation algorithm in multi-probe anechoic chamber, and unmanned aerial vehicle air-to-ground radio propagation.

Troels Pedersen received the M.Sc. degree in digital communications and the Ph.D. degree in wireless communications from Aalborg University, Aalborg, Denmark, in 2004 and 2009, respectively. He has been with the Department of Electronic Systems, Aalborg University, since 2009, as an Assistant Professor, and since 2012, as an Associate Professor. In 2012, he was a Visiting Professor with Institut d'Electronique et la Telecommunications de Rennes, University of Rennes 1, Rennes, France. His current research interests are within statistical signal processing and communication theory, including sensor array signal processing, radio geolocation techniques, radio channel modeling, and radio channel sounding. He was the recipient of the Teacher of the Year Award twice by the Study Board for Electronics and IT, Aalborg University, in 2011 and 2017, respectively.

Mingming Gan received the B.Sc. degree in electronic information engineering from Minzu University of China, China in 2007. She received the M.Sc. degree in wireless communications from Lund University, Sweden in 2010, with her Master Thesis written at the FTW Telecommunications Research Center Vienna, Austria. In 2015, she received her Ph.D. degree with distinction in engineering sciences from Vienna University of Technology, Austria. From 2010 to 2015, she was with the FTW Telecommunications Research Center Vienna working as a researcher in the "Signal and Information Processing" department. After working at AIT Austrian Institute of Technology as a researcher in the research group for ultra-reliable wireless machine-to-machine communications, Mingming joined Shanghai Huawei Technologies as a senior engineer in 2016. Her research interests are in the fields of modeling of wireless propagation channels, indoor channel characterization for high-speed short-range systems, time-variant vehicle-to-vehicle communications, time-variant fast fading statistics and diffuse scattering algorithms.

Evgenii Vinogradov received the Dipl. Engineer degree in Radio Engineering and Telecommunications from Saint-Petersburg Electrotechnical University (Russia), in 2009. After several years of working in the field of mobile communications, he joined UCL (Belgium) in 2013, where he obtained his Ph.D. degree in 2017. His doctoral research interests focused on radio propagation channel modeling. In 2017, Evgenii joined the electrical engineering department at Katholieke Universiteit Leuven (Belgium) where he is working on wireless communications with Unmanned Aerial Vehicles.

Claude Oestges received the M.Sc. and Ph.D. degrees in Electrical Engineering from the Université Catholique de Louvain (UCLouvain), Louvain-la-Neuve, Belgium, respectively in 1996 and 2000. In January 2001, he joined as a post-doctoral scholar the Smart Antennas Research Group (Information Systems Laboratory), Stanford University, CA, USA. From January 2002 to September 2005, he was associated with the Microwave Laboratory UCLouvain as a post-doctoral fellow of the Belgian Fonds de la Recherche Scientifique (FRS-FNRS). Claude Oestges is presently Full Professor with the Electrical Engineering Department, Institute for Information and Communication Technologies, Electronics and Applied Mathematics (ICTEAM), UCLouvain. He currently chairs COST Action CA15104 IRACON (2016-2020). He is the author or co-author of three books and more than 200 journal papers and conference communications, and was the recipient of the 1999-2000 IET Marconi Premium Award and of the IEEE Vehicular Technology Society Neal Shepherd Award in 2004 and 2012.